Information Timeliness Aware Multispectral Integrated Sensing, Communication, and Computing for High-Voltage Discharge Detection

Haijun Liao, *Student Member, IEEE,* Zijia Yao, Jiaxuan Lu, Yiling Shu, Zhenyu Zhou, *Senior Member, IEEE,* and Shahid Mumtaz, *Senior Member, IEEE*

***Abstract*—The application of multispectral image based partial discharge detection offers a dependable solution for high-voltage substations. Captured visible light and ultraviolet (UV) images are denoised, transmitted and fused to enhance detection performance. However, existing approaches separately design the sensing-layer image denoising, communication-layer image transmission, and computing-layer image fusion, and the lack of unified cooperation hinders the overall performance. To address this issue, it is crucial to integrate sensing, communication, and computing to improve detection accuracy and timeliness. In this paper, we formulate a timeliness and accuracy joint guarantee problem, which aims to minimize the weighted sum of peak age of information (AoI), false-positive detection ratio, and false-negative detection ratio by jointly optimizing sensing-layer filtering window size, communication-layer time division ratio, and computing layer wavelet decomposition level. We propose a multispectral integrated sensing, communication, and computing algorithm based on AoI and false-negative aware multi-experience replay cooperative learning to solve the problem. Simulation results demonstrate that the proposed algorithm outperforms existing methods in terms of peak AoI, false-positive detection ratio, false-negative detection ratio, and convergence speed.**

***Index Terms*—high-voltage partial discharge detection, multispectral image detection, AoI, multi-experience replay cooperative learning, sensing-communication-computing integration**

I. Introduction

Partial discharge causes significant damages to high-voltage substations and even results in breakdown of power grid. It is caused by insulation aging and dampness, and contains various types including corona discharge, arc discharge, surface discharge, and air gap discharge [1]. Partial discharge detection is crucial for ensuring the safe and stable operation of power grid. Among various detection methods, multispectral image based partial discharge detection has demonstrated great advantages of electromagnetic immunity and high sensitivity. It combines both visible light and ultraviolet (UV) light to enable identification and localization of partial discharge sources. Specifically, UV image reveals discharge existence by examining radiation in the UV band, while the visible light image offers background information for discharge localization. The key processes include image capture, denoising, transmission, fusion and detection, which involve sensing layer, communication layer, and computing layer. However, these three key layers are generally designed separately and lack unified cooperation, which leads to unignorable performance degradation. Therefore, it is an urgent task to improve detection performance by integrating sensing, communication, and computing.

Partial discharge detection requires timely image information [2], which indicates how closely the images match the actual state. Although delay has been widely utilized to measure timeliness, it only reflects the duration of single frame transmission. A better metric is information timeliness. Compared with delay, information timeliness spans the entire life cycle of image sensing, transmission, processing, and detection, which is critical for realizing real-time detection. It is important to guarantee information timeliness awareness in the design of multispectral integrated sensing, communication, and computing. Some major technical challenges need to be tackled.

First, multispectral integrated sensing, communication, and computing requires the collaboration between device-side image denoising and transmission, and edge-side image fusion and partial discharge detection. It involves the joint optimization of median filtering window size, time division ratio, and wavelet decomposition level, which is a mixed integer programming problem and NP-hard. Second, timeliness and accuracy are a pair of paradox metrics. False-positive and false-negative detection ratios are common metrics of detection accuracy, which are closely related with image denoising and fusion. Utilizing more complex image denoising and fusion mechanisms can increase accuracy but inevitably reduces timeliness. In addition, information timeliness guarantee from long-term perspective is challenging due to the coupling between states and decisions cross time slots [3]. Last but not least, the lack of collaboration among sensing, communication, and computing leads to bound violations of information timeliness and false-negative ratio. These failure experiences of bound violations contain rich information of how to guarantee detection timeliness and accuracy but are generally ignored by classical learning methods such as deep Q-network (DQN) and deep actor critic (DAC). It requires thorough investigation on how to cooperatively learn from

H. Liao, Z. Yao, J. Lu, Y. Shu, and Z. Zhou are with the State Key Laboratory of Alternate Electrical Power System with Renewable Energy Sources, School of Electrical and Electronic Engineering, North China Electric Power University, Beijing, China, 102206 (E-mail: {haijun_liao, zijia_yao, lujiaxuan_lu, yiling_shu, zhenyu_zhou}@ncepu.edu.cn). *Corresponding author: Zhenyu Zhou*.

S. Mumtaz is with Department of Applied Informatics, Silesian University of Technology, Akademicka, 16 44-100, Gliwice, Poland, and Departement of Engineering, Nottingham Trent University (E-mail: dr.shahid.mumtaz@ieee.org).

both success and failure experiences for joint guarantee of timeliness and accuracy.

There exist several works on integrated sensing, communication, and computing. In [4], Wang *et al*. formulated a computation rate maximization problem and proposed an alternating direction method of multipliers-based alternating optimization algorithm to solve it. In [5], Qi *et al*. proposed a unified framework integrating sensing, communication, and computing to optimize limited resources for wireless networks. However, the aforementioned works do not consider information timeliness guarantee for multispectral image-based partial discharge detection.

Age of information (AoI) is an effective indicator to measure information timeliness. A smaller AoI reflects more consistency between detected image and actual partial discharge state [6]. Some scholars have studied coordinated resource management from the perspective of AoI minimization. In [7], Hu *et al.* designed a dynamic programming and ant colony heuristic algorithm to minimize the average AoI of data collected by internet of things devices. In [8], Sinha *et al.* proposed two greedy scheduling policies, i.e., total AoI minimization and jitter minimization, to improve network stability. However, these studies ignore the contradiction between timeliness and accuracy encountered in partial discharge detection. AoI is reduced at the cost of increased ratios of false-positive and false-negative detection.

Deep reinforcement learning has been widely adopted to address complex network management problem involving collaboration among multiple layers. It combines the advantages of deep neural networks in feature extraction and reinforcement learning in multivariable collaborative optimization [9]. In [10], Liu *et al.* proposed a DQN-based scheme to find the near-optimal solution that minimizes the average AoI of the system. In [11], Li *et al.* proposed an AoI-aware scheduling scheme based on DAC and primal-dual optimization to optimize the data rate performance under AoI constraint. However, these works have not investigated the cooperation between success and failure experience replay. Moreover, since classical DQN and DAC are inefficient to simultaneously handle continuous and integer variables, they adopt variable discretization which results in unignorable performance loss [12], [13].

Motivated by these challenges, we first construct a model for multispectral integrated sensing, communication, and computing for high-voltage partial discharge detection with multispectral images. Then, we formulate the timeliness and accuracy joint guarantee problem. The objective is to minimize the weighted sum of peak AoI, the ratio of false-positive detection, and the ratio of false-negative detection by jointly optimizing sensing-layer filtering window size, communication-layer time division ratio, and computing-layer wavelet decomposition level. Finally, a multispectral integrated sensing, communication, and computing algorithm based on AoI and false negative aware multi-experience replay cooperative learning is proposed to solve the problem. The main contributions are summarized as follows.

- *Integrated sensing, communication, and computing for multispectral image empowered partial discharge detection*: We construct a framework of integrated sensing, communication, and computing for partial discharge detection based on multispectral images. The sensing layer realizes image denoising based on the proposed improved median filtering. The communication layer performs transmission of visible light and UV images based on time division multiplexing (TDM). The computing layer implements image fusion and partial discharge detection by combining intensity-hue-saturation (IHS), wavelet transform and Canny edge detection operator. Integrated sensing, communication, and computing is achieved by jointly optimizing sensing-layer filtering window size, communication-layer time division ratio, and computing-layer wavelet decomposition level.
- *Joint guarantee of detection timeliness and accuracy*: We develop peak AoI to characterize timeliness, and employ the ratios of false-positive and false-negative detection to characterize accuracy. Then, timeliness and accuracy are jointly guaranteed from two aspects. On the one hand, the objective is defined as a weighted sum of peak AoI, false-positive detection ratio, and false-negative detection ratio based on multi-objective optimization. By adjusting the weights, we can strike the right balance between timeliness and accuracy. After problem transformation, AoI virtual deficit queue backlog is minimized to ensure long-term guarantee of AoI. On the other hand, the proposed algorithm is augmented with AoI and false-negative awareness to avoid AoI bound violation and false-negative detection occurrence.
- *Improved learning based on DAC-DQN cooperation as well as success-failure experience replay cooperation*: The proposed learning algorithm contains two cooperative state spaces. The continuous outputs of DAC in terms of time division ratios are forwarded as the input of DQN and incorporated into its state space. Then, integer optimization decisions of filter window size and wavelet decomposition layer are made by the augmented DQN. We further propose multi-experience replay pools and adaptive mini-batch extraction to facilitate cooperative learning. Success and failure experiences are extracted and combined to construct a new mini-batch. The cooperative extraction ratio is dynamically adjusted to increase convergence rate and reduce probabilistic AoI bound violation and false-negative detection occurrence.

The rest of this paper is organized as follows. Section II describes the system model of multispectral image empowered partial discharge detection. The joint guarantee problem of timeliness and accuracy is formulated in Section III. Section IV elaborates the proposed integration algorithm. Section V presents simulation results. Finally, Section VI concludes this paper.

II. System Model

The framework of information timeliness-aware integration of multispectral sensing, communication, and computing for high-voltage discharge detection is shown in Fig. 1. It consists of three layers introduced as follows.

The sensing layer realizes image acquisition and denoising. A multispectral camera is deployed to capture visible light

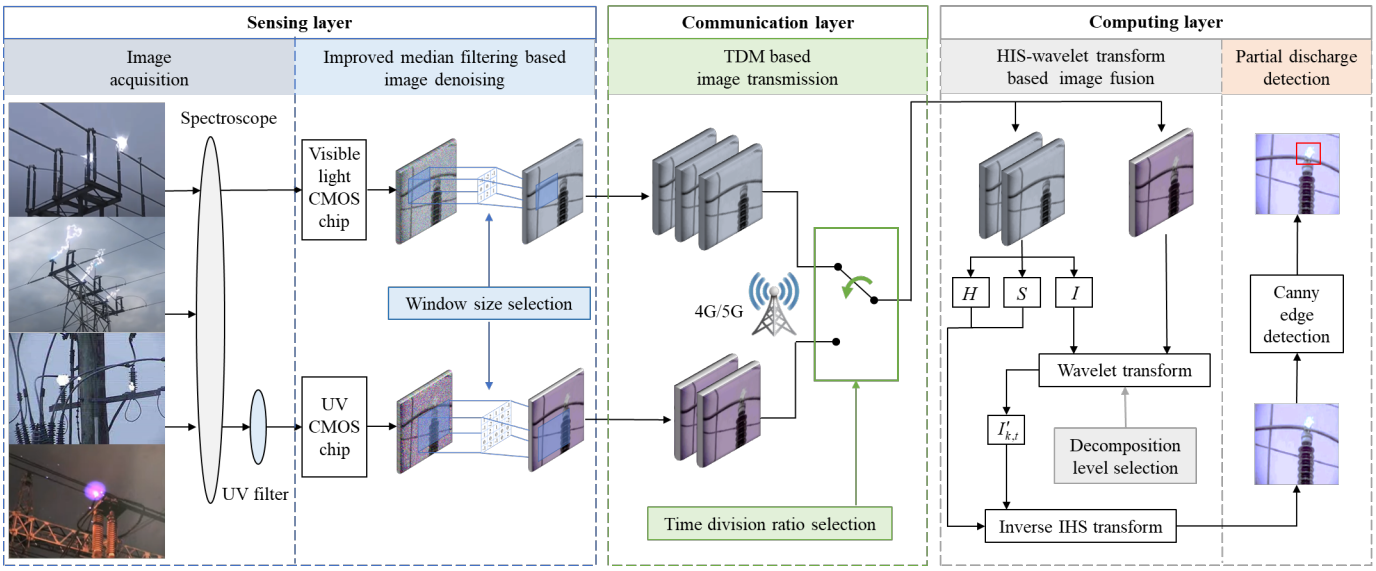

Fig. 1. Information timeliness-aware integration of multispectral sensing, communication, and computing for high-voltage discharge detection

TABLE I
NOMENCLATURE

Notation	Description	Notation	Description
$\Theta_s^l(t)$	Sensing queue backlog of visible light image	$\Theta_s^u(t)$	Sensing queue backlog of UV image
$S^l(t)$	Denoised frames of visible light image	$S^u(t)$	Denoised frames of UV image
$K(t)$	Frames of captured visible light and UV images	$O(t)$	Frames of fused images
$\tau_s^{l,q}(t)$	Queuing delay of denoising visible light image	$\tau_s^{u,q}(t)$	Queuing delay of denoising UV image
$\Theta_{Tx}^l(t)$	Communication queue backlog for visible light image	$\Theta_{Tx}^u(t)$	Communication queue backlog for UV image
$C^l(t)$	Transmitted frames of visible light image	$C^u(t)$	Transmitted frames of UV image
$\tau_{Tx}^{l,q}(t)$	Queuing delay of visible light image transmission	$\tau_{Tx}^{u,q}(t)$	Queuing delay of UV image transmission
$\Theta_c^l(t)$	Computing queue backlog for visible light image	$\Theta_c^u(t)$	Computing queue backlog for UV image
$\tau_c^{l,q}(t)$	Queuing delay of visible light image fusion	$\tau_c^{u,q}(t)$	Queuing delay of UV image fusion
$FP(t)$	False-positive detection ratio	$FN(t)$	False-negative detection ratio
$\tau_c(t,k)$	Image fusion delay of the k-th frame in slot t	$\tau_d(t,k)$	Detection delay of the k-th frame in slot t
$\tau(t,k)$	End-to-end delay of the k-th frame in slot t	$PAoI(t,k)$	Peak AoI of the k-th frame in slot t
$PAoI(t)$	Peak AoI in slot t	$AD(t)$	Virtual deficit queue backlogs of C_{10}
$G_s^l(t)$	Virtual deficit queue backlogs of C_4	$G_s^u(t)$	Virtual deficit queue backlogs of C_5
$G_{Tx}^l(t)$	Virtual deficit queue backlogs of C_6	$G_{Tx}^u(t)$	Virtual deficit queue backlogs of C_7
$G_c^l(t)$	Virtual deficit queue backlogs of C_8	$G_c^u(t)$	Virtual deficit queue backlogs of C_9

and UV images of partial discharge. The light is divided into two beams through the spectroscope, which are converted into visible light image and UV image through visible light and UV CMOS chips, respectively. Afterwards, improved median filtering is performed to achieve image denoising. In the communication layer, the denoised data of visible light and UV images are transmitted from camera to edge server in TDM through 4G/5G. In the computing layer, received visible light and UV images are fused based on IHS-wavelet transform. Then, partial discharge detection is performed based on Canny edge detection. The goal is to achieve information timeliness-aware multispectral integrated sensing, communication, and computing for high-voltage discharge detection. It is necessary to optimize the parameters of both visible light and UV images because they are processed independently by separate CMOS chips but are fused in the end to improve detection performance. We employ AoI to characterize detection timeliness, while detection accuracy is measured based on the ratios of false-positive and false-negative detection. For ease of reference, we list the key notations of this paper in Table I.

A. Sensing Layer Model

1) Image denoising model: To denoise salt and pepper noise (SPN) and Gaussian noise, we combine median filtering and mean filtering to propose an improved median filtering algorithm. This algorithm assigns weights to each pixel centered around the median pixel and calculates the weighted sum as the filter output. The steps are introduced as follows.

Window size selection of improved median filtering: We consider a discrete slot model with T slots. The set is defined as $\mathcal{T}$ and the slot length is τ. In each slot, $K(t)$ frames of visible light images and $K(t)$ frames of UV images are captured. Take the k-th frame UV image in slot t as an example. Assume that the coordinate of pixel to be filtered is

(x, y) and its gray level is denoted as $I_k^u(x, y, t)$. Construct a window centered at (x, y) to perform median filtering on all pixels within the window. Since visible light and UV images are processed at separate CMOS chips, different filter window sizes are adopted to enhance denoising performance. Define the window sizes of visible light and UV images as $w^l(t), w^u(t) \in \mathcal{W} = \{W_{\min}, \cdots, W, \cdots, W_{\max}\}$, and $\mathcal{W}$ is a set of odd numbers. As shown in Fig. 1, $w^l(t) = 3$ and $w^u(t) = 5$ indicate that the window sizes for visible light and UV images are 3×3 and 5×5, respectively. For example, $w^u(t) = W$ represents that the window size is $W \times W$. In practical implementation, W is selected by the proposed algorithm. $W_{\min}$ and $W_{\max}$ are the minimum and maximum window sizes, respectively.

Pixel weight calculation: Derive the median pixel (i_0, j_0) by sorting $W \times W$ pixels within the window based on gray level. The weight assigned to each pixel around (i_0, j_0) in the k-th frame of UV image is given by

$$\rho_k^u(i, j, t) = \frac{1/(1 + (D_k^u(i, j, t))^2)}{\sum_{i=x-W^*}^{x+W^*} \sum_{j=y-W^*}^{y+W^*} [1/(1 + (D_k^u(i, j, t))^2)]}. \tag{1}$$

$\rho_k^u(i, j, t)$ is negatively proportional to the difference between gray levels, i.e., $D_k^u(i, j, t) = I_k^u(i, j, t) - I_k^u(i_0, j_0, t)$. $W^* = \lfloor W/2 \rfloor$, and $\lfloor \cdot \rfloor$ represents rounding down.

Output of improved median filtering: The output is the weighted sum of gray levels of all pixels within the filtering window, which is given by

$$I_{s,k}^u(x, y, w^u(t)) = \sum_{i=x-W^*}^{x+W^*} \sum_{j=y-W^*}^{y+W^*} \rho_k^u(i, j, t) I_k^u(i, j, t). \tag{2}$$

The improved median filtering for visible light images is performed similarly.

2) Sensing-layer data queue model: Define $\Theta_s^l(t)$ and $\Theta_s^u(t)$ as sensing data queues for visible light and UV images, respectively. As shown in Fig. 2, the frames of captured visible light images and UV images $K(t)$ are the inputs of $\Theta_s^l(t)$ and $\Theta_s^u(t)$. The denoised frames of visible light images $S^l(t)$ and UV images $S^u(t)$ are the outputs. The queue backlogs of $\Theta_s^l(t)$ and $\Theta_s^u(t)$ are given by

$$\Theta_s^l(t + 1) = [\Theta_s^l(t) + K(t) - S^l(t)]^+, \tag{3}$$
$$\Theta_s^u(t + 1) = [\Theta_s^u(t) + K(t) - S^u(t)]^+, \tag{4}$$

where $[\cdot]^+$ represents $\max[\cdot, 0]$. $S^l(t)$ and $S^u(t)$ are derived as

$$S^l(t) = \left\lfloor \frac{\tau f_s^l(t)}{C_s^l(w^l(t))} \right\rfloor, \tag{5}$$
$$S^u(t) = \left\lfloor \frac{\tau f_s^u(t)}{C_s^u(w^u(t))} \right\rfloor, \tag{6}$$

where $f_s^l(t)$ and $f_s^u(t)$ represent the computing resources used for visible light and UV image denoising, respectively. $C_s^l(w^l(t))$ and $C_s^u(w^u(t))$ represent the computation complexity of denosing, which are related to the window size.

Based on the Little's Law [14], the queuing delays of denoising visible light and UV images are given by

$$\tau_s^{l,q}(t) = \frac{\Theta_s^l(t + 1)}{\tilde{K}(t + 1)}, \tag{7}$$
$$\tau_s^{u,q}(t) = \frac{\Theta_s^u(t + 1)}{\tilde{K}(t + 1)}, \tag{8}$$

where $\tilde{K}(t) = \frac{1}{t-1} \sum_{m=1}^{t-1} K(m)$ represents the average data arrival rate. Since sensing data queues for visible light and UV images have consistent inputs $K(t)$ in all slots, the same notation can be used to represent the average data arrival rate of denoising visible light and UV images.

B. Communication Layer Model

Define $\Theta_{Tx}^l(t)$ and $\Theta_{Tx}^u(t)$ as communication data queues for visible light and UV images, respectively. As shown in Fig. 2, the outputs of sensing data queues $S^l(t)$ and $S^u(t)$ are the inputs of $\Theta_{Tx}^l(t)$ and $\Theta_{Tx}^u(t)$, respectively. The transmitted frames of visible light images $C^l(t)$ and UV images $C^u(t)$ are the outputs. The queue backlogs of $\Theta_{Tx}^l(t)$ and $\Theta_{Tx}^u(t)$ are given by

$$\Theta_{Tx}^l(t + 1) = [\Theta_{Tx}^l(t) + S^l(t) - C^l(t)]^+, \tag{9}$$
$$\Theta_{Tx}^u(t + 1) = [\Theta_{Tx}^u(t) + S^u(t) - C^u(t)]^+. \tag{10}$$

Denoised images are transmitted to the edge server based on TDM, which possesses the advantages of low complexity and strong anti-interference capability. Define $\delta^l(t)$ and $\delta^u(t)$ as the time division ratios of visible light and UV images, which satisfy $\delta^l(t) + \delta^u(t) = 1$, $\delta^l(t), \delta^u(t) \in [0, 1]$. $C^u(t)$ and $C^l(t)$ are given by

$$C^l(t) = \arg\max_K \left(\delta^l(t) \tau R(t) - \sum_{k=1}^{K} A_c^l(t, k) \geq 0 \right), \tag{11}$$
$$C^u(t) = \arg\max_K \left(\delta^u(t) \tau R(t) - \sum_{k=1}^{K} A_c^u(t, k) \geq 0 \right), \tag{12}$$

where $A_c^l(t, k)$ and $A_c^u(t, k)$ respectively represent the data sizes of the k-th frame visible light and UV images. $R(t)$ represents the data transmission rate derived based on Shannon capacity. In (11), $\delta^l(t)\tau R(t)$ represents the maximum amount of data allowed to be transmitted for visible light images in slot t, and $\sum_{k=1}^{K} A_c^l(t, k)$ represents the total data size of K frames of visible light images. The maximum transmitted frame K should satisfy the condition $\delta^l(t)\tau R(t) - \sum_{k=1}^{K} A_c^l(t, k) \geq 0$. Equation (12) is calculated similarly as (11).

The queuing delays of visible light and UV image transmission in the communication layer are given by

$$\tau_{Tx}^{l,q}(t) = \frac{\Theta_{Tx}^l(t + 1)}{\tilde{S}^l(t + 1)}, \tag{13}$$
$$\tau_{Tx}^{u,q}(t) = \frac{\Theta_{Tx}^u(t + 1)}{\tilde{S}^u(t + 1)}, \tag{14}$$

where $\tilde{S}^l(t) = \frac{1}{t-1} \sum_{m=1}^{t-1} S^l(m)$ and $\tilde{S}^u(t) = \frac{1}{t-1} \sum_{m=1}^{t-1} S^u(m)$ represent the average data arrival rates of denoised visible light and UV images.

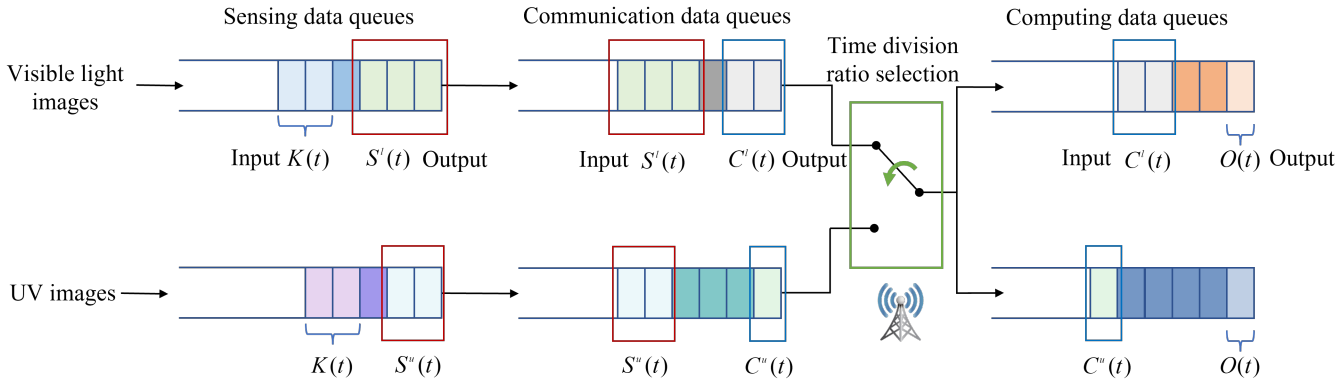

Fig. 2. Backlog evolution of sensing data queues, communication data queues, and computing data queues.

C. Computing Layer Model

In the computing layer, edge server fuses the received visible light and UV images to detect partial discharge.

1) IHS-wavelet transform based image fusion: Image fusion is performed based on the proposed IHS-wavelet transform as shown in Fig. 3. It incorporates fast fusion of IHS transform and strong information extraction ability of wavelet transform.

IHS Transform: Transfer the visible light image from red, green and blue (RGB) space into IHS space to obtain intensity (I), hue (H) and saturation (S) components.

Wavelet Decomposition: Perform wavelet decomposition to decompose UV image into four components, i.e., low-low (LL), high-low (HL), low-high (LH), and high-high (HH). Define $d(t)$ as the wavelet decomposition level in slot t, $d(t) \in \mathcal{D} = \{d_{\min}, \cdots, d_{\max}\}$, where $d_{\min}$ and $d_{\max}$ are the minimum and maximum wavelet decomposition levels. For the n-th level, $n \leq d(t)$, define the coefficient matrices of LL, HL, LH, and HH as Z_n, B_n^H , B_n^V, and B_n^D, which are given by

$$\begin{cases} Z_n = L_r \cdot L_c \cdot Z_{n-1}, \\ B_n^H = H_r \cdot L_c \cdot Z_{n-1}, \\ B_n^V = L_r \cdot H_c \cdot Z_{n-1}, \\ B_n^D = H_r \cdot H_c \cdot Z_{n-1}, \end{cases} \tag{15}$$

where L_r and H_r are filters operated on row, and L_c and H_c are filters operated on column. Apply (15) to I component of visible light image in a similar way to realize wavelet decomposition.

Coefficient combination: Combine the coefficients corresponding to each component at the same level in the I component of visible light image and UV image. The high-frequency coefficients corresponding to HL, LH, and HH components are combined based on max-selection method to extract more image details. Low-frequency coefficients corresponding to LL component are combined based on averaging method to improve stability.

Wavelet reconstruction: Perform wavelet reconstruction in each level to obtain a new LL component. The wavelet reconstruction in level $d(t)$ is given by

$$\begin{aligned} Z_{d(t)-1} = \bar{L}_r \bar{L}_c Z_{d(t)} + \bar{L}_r \bar{H}_c B_{d(t)}^H \\ + \bar{H}_r \bar{L}_c B_{d(t)}^V + \bar{H}_r \bar{H}_c B_{d(t)}^D, \end{aligned} \tag{16}$$

where $\bar{[\cdot]}$ represents conjugate transpose operation. Repeat (16) for $d(t)$ times, and obtain the new I component $\mathrm{I}'_{k,t}$.

Inverse IHS transform: Transform $\mathrm{I}'_{k,t}$ together with $\mathrm{H}_{k,t}$ and $\mathrm{S}_{k,t}$ components back into RGB space to obtain the fused image.

2) Computing-layer data queue model: Define $\Theta_c^l(t)$ and $\Theta_c^u(t)$ as computing data queues for visible light and UV images, respectively. As shown in Fig. 2, the outputs of communication data queues $C^l(t)$ and $C^u(t)$ are the inputs of $\Theta_c^l(t)$ and $\Theta_c^u(t)$. The frames of fused images $O(t)$ are the outputs. The queue backlogs of $\Theta_c^l(t)$ and $\Theta_c^u(t)$ evolve as

$$\Theta_c^l(t+1) = [\Theta_c^l(t) + C^l(t) - O(t)]^+, \tag{17}$$

$$\Theta_c^u(t+1) = [\Theta_c^u(t) + C^u(t) - O(t)]^+. \tag{18}$$

$O(t)$ depends on the wavelet decomposition level $d(t)$, which is given by

$$O(t) = \arg\max_K \left(\tau - \sum_{k=1}^{K} \tau_c(t,k) \geq 0 \right). \tag{19}$$

$\tau_c(t,k)$ represents the image fusion delay, which is derived as

$$\tau_c(t,k) = \frac{C^{com}(k, d(t)) A_c(t,k)}{f_c(t)}, \tag{20}$$

where $f_c(t)$ represents the computing resources for image fusion. $A_c(t,k)$ represents the data size of the k-th frame image to be fused. $C^{com}(k, d(t))$ represents the computation complexity of image fusion associated with $d(t)$.

The queuing delays of visible light and UV image fusion in the computing layer are given by

$$\tau_c^{l,q}(t) = \frac{\Theta_c^l(t+1)}{\tilde{C}^l(t+1)}, \tag{21}$$

$$\tau_c^{u,q}(t) = \frac{\Theta_c^u(t+1)}{\tilde{C}^u(t+1)}, \tag{22}$$

where $\tilde{C}^l(t) = \frac{1}{t-1} \sum_{m=1}^{t-1} C^l(m)$ and $\tilde{C}^u(t) = \frac{1}{t-1} \sum_{m=1}^{t-1} C^u(m)$ represent the average data arrival rates of transmitted visible light and UV images.

3) Canny edge-based partial discharge detection: After image fusion, partial discharge detection is performed based on Canny edge detection.

First, the UV image is converted into a gray image, which is binarized to obtain the binary image. The Canny operator is used to detect the edge of the binary image and determine the light spot region. Then, the area of the light spot region is calculated. When the area exceeds the threshold ζ, it is determined as a fault region. Based on the coordinates of the edge points in faulty region that obtained from UV image, the faulty region is localized in the fused image. In this way, the location and extent of partial discharge fault can be clearly identified in fused image.

We use ratios of false-positive and false-negative detection to measure the accuracy of partial discharge detection. False-positive detection represents that a normal image is misjudged as faulty. False-negative detection represents that a faulty image is misjudged as normal. Define the numbers of detected frames with false-positive and false-negative faults in slot t as $O_{FP}(t)$ and $O_{FN}(t)$, which can be observed at the end of slot t. The ratios of false-positive detection and false-negative detection are calculated as

$$FP(t) = \frac{O_{FP}(t)}{O(t)}, \tag{23}$$

$$FN(t) = \frac{O_{FN}(t)}{O(t)}. \tag{24}$$

Define $\tau_d(t,k)$ as the detection delay for the k-th frame fused image in slot t, which is given by

$$\tau_d(t,k) = \frac{C^{det}(t,k)A_d(t,k)}{f_d(t)}, \tag{25}$$

where $f_d(t)$ represents the computing resources for Canny edge detection, $A_d(t,k)$ represents the data size of the k-th frame fused image, and $C^{det}(t,k)$ represents the computation complexity of detecting the k-th frame fused image in slot t.

Our model is compatible with other algorithms of image denoising and fusion because none specific assumption is imposed on the queue model, image data size, and channel state. For example, the proposed communication layer model can be easily extended to frequency division multiplexing (FDM) by replacing variables of time division ratio with bandwidth allocation ratios. Consequently, the adoption of different algorithms or mechanisms only impacts the queue inputs and outputs, and the new problem can be easily solved by the proposed algorithm with little modification.

D. AoI Model

AoI is defined as the existence duration extending from the capture time of the last image used for detection to the current time. Define $\tau(t,k)$ as the end-to-end delay of the k-th frame. As shown in Fig. 4, the initial AoI of the k-th frame in the t-th slot is $\tau(t,k)$. AoI keeps increasing, i.e., information becomes aging, until the $(k+1)$-th image has been detected. Afterwards, information is renewed, and AoI is initialized to the end-to-end delay of the next-frame image experienced from capture

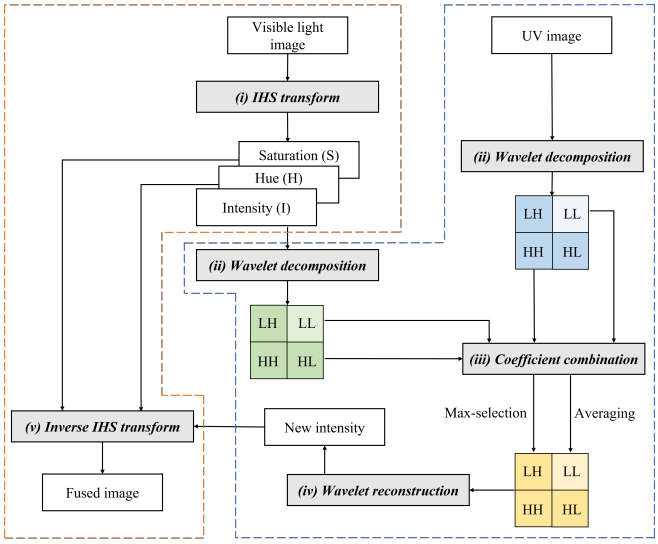

Fig. 3. Flow of image fusion.

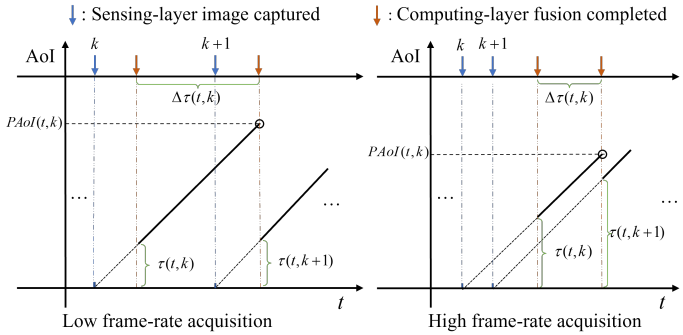

Fig. 4. Evolution of AoI.

to detection, i.e., $\tau(t,k+1)$. Therefore, the peak AoI of the k-th frame is given by

$$PAoI(t,k) = \tau(t,k) + \Delta\tau(t,k), \tag{26}$$

where $\Delta\tau(t,k)$ is the time interval between detection of the k-th frame and that of the next frame.

Fig. 4 presents two cases of AoI evolution. The first case represents a typical scenario of high frame-rate capture where the $(k+1)$-th frame is already in the computing data queue. $\Delta\tau(t,k)$ equals to the delay of image fusion $\tau_c(t,k+1)$. The second case represents a typical scenario of low frame-rate capture where the $(k+1)$-th frame is captured after the detection of the k-th frame. $\Delta\tau(t,k)$ depends on image capture interval and end-to-end delay. Under these two cases, $\Delta\tau(t,k)$ is modeled as

$$\Delta\tau(t,k) = \begin{cases} \tau_c(t,k+1), \\ \qquad \text{high frame-rate case}, \\ \frac{\tau}{K(t-1)} - \tau(t-1, O(t-1)) + \tau(t,k), \\ \qquad \text{low frame-rate case}, k = 1, \\ \frac{\tau}{K(t)} - \tau(t,k-1) + \tau(t,k), \\ \qquad \text{low frame-rate case}, k \neq 1, \end{cases} \tag{27}$$

Based on (26) and (27), the peak AoI of the k-th frame, i.e., $PAoI(t,k)$, includes the end-to-end delay, which is not only related to sensing-layer queuing delay, but also related to communication-layer queuing delay and computing-layer queuing delay and detection delay. Therefore, the slot-index $PAoI(t,k)$ is different across both frame and slot. The peak AoI in the t-th slot depends on the largest peak AoI over $O(t)$ frames, which is given by

$$PAoI(t) = \max_{k=1,2,\cdots,O(t)} \{PAoI(t,k)\} \tag{28}$$

From (26) and (27), it is intuitive that increasing frame rate $\frac{K(t)}{\tau}$ can reduce $\frac{\tau}{K(t-1)}$ in the low frame-rate case, thereby reducing peak AoI. However, this is not always valid since high frame-rate also incurs larger end-to-end delay. Particularly, the capacities of denoising, communication, and image fusion jointly determine the peak AoI. Therefore, it is important to minimize AoI by jointly optimizing sensing, communication, and computing.

Remark 1. AoI and end-to-end delay are not exactly the same. Reducing end-to-end delay is beneficial for peak AoI reduction to a certain degree, but AoI keeps rising if no new frame occurs.

Remark 2. Although using images with smaller AoI reduces false positive and false negative, AoI minimization is not necessarily consistent with detection accuracy improvement. For example, increasing filtering window size and wavelet decomposition level results in higher accuracy, but also increases end-to-end delay and peak AoI.

Remark 3. Low end-to-end delay is achieved at the cost of resource redundancy, which are thus not equivalent to low AoI guarantee. Specifically, redundant storage, communication, and computing resources are not fully utilized to transmit useful information as much as possible, which results in high AoI.

III. Problem Formulation

In this paper, we address timeliness and accuracy joint guarantee problem of partial discharge detection with multispectral images. The objective is to minimize the weighted sum of peak AoI, the ratio of false-positive detection, and the ratio of false-negative detection by jointly optimizing sensing-layer filtering window size, communication-layer time division ratio, and computing-layer wavelet decomposition level. Considering dynamic image data arrivals and departures of sensing, communication, and computing layers, we investigate the optimization of time-average peak AoI over T slots, which makes the proposed model more suitable for practical applications with stochastic network characteristic and unignorable queue backlogs. We also consider a series of long-term constraints of AoI and queuing delay. The optimization problem is formulated as

$$\begin{aligned}
\mathbf{P1}: & \min_{\{w^l(t),w^u(t),\delta^l(t),\delta^u(t),d(t)\}} \frac{1}{T}\sum_{t=1}^{T}\Big\{\alpha_1 PAoI(t) \\
& + \alpha_2 FP(t) + \alpha_3 FN(t)\Big\}, \\
\text{s.t. } & C_1: w^l(t), w^u(t) \in \mathcal{W}, \forall t \in \mathcal{T}, \\
& C_2: \delta^l(t), \delta^u(t) \in [0,1], \delta^l(t)+\delta^u(t)=1, \forall t \in \mathcal{T}, \\
& C_3: d(t) \in \mathcal{D}, \forall t \in \mathcal{T}, \\
& C_4: \lim_{T\to\infty}\frac{1}{T}\sum_{t=1}^{T}\frac{\Theta_s^l(t)}{\tilde{K}(t)} \leqslant \tau_{s,\max}^{l,q}, \\
& C_5: \lim_{T\to\infty}\frac{1}{T}\sum_{t=1}^{T}\frac{\Theta_s^u(t)}{\tilde{K}(t)} \leqslant \tau_{s,\max}^{u,q}, \\
& C_6: \lim_{T\to\infty}\frac{1}{T}\sum_{t=1}^{T}\frac{\Theta_{Tx}^l(t)}{\tilde{S}^l(t)} \leqslant \tau_{Tx,\max}^{l,q}, \\
& C_7: \lim_{T\to\infty}\frac{1}{T}\sum_{t=1}^{T}\frac{\Theta_{Tx}^u(t)}{\tilde{S}^u(t)} \leqslant \tau_{Tx,\max}^{u,q}, \\
& C_8: \lim_{T\to\infty}\frac{1}{T}\sum_{t=1}^{T}\frac{\Theta_c^l(t)}{\tilde{C}^l(t)} \leqslant \tau_{c,\max}^{l,q}, \\
& C_9: \lim_{T\to\infty}\frac{1}{T}\sum_{t=1}^{T}\frac{\Theta_c^u(t)}{\tilde{C}^u(t)} \leqslant \tau_{c,\max}^{u,q}, \\
& C_{10}: \lim_{T\to\infty}\frac{1}{T}\sum_{t=1}^{T} PAoI(t) \leqslant AoI_{\max},
\end{aligned} \tag{29}$$

where α_1, α_2, and α_3 are the wights of AoI, false-positive ratio, and false-negative ratio, respectively, which represent the dominance of a particular metric on the entire optimization objective. Therefore, the weights should be carefully determined to ensure that the weighted $PAoI(t)$, $FP(t)$, and $FN(t)$ are in the same order of magnitude. C_1 is the sensing constraint on filtering window size. C_2 is the communication constraint on time division ratio. C_3 is the computing constraint on wavelet decomposition level. $C_4 \sim C_9$ are queuing delay constraints, where $\tau_{s,\max}^{l,q}$, $\tau_{s,\max}^{u,q}$, $\tau_{Tx,\max}^{l,q}$, $\tau_{Tx,\max}^{u,q}$, $\tau_{c,\max}^{l,q}$, and $\tau_{c,\max}^{u,q}$ represent the queuing delay thresholds of $\Theta_s^l(t)$, $\Theta_s^u(t)$, $\Theta_{Tx}^l(t)$, $\Theta_{Tx}^u(t)$, $\Theta_c^l(t)$, and $\Theta_c^u(t)$, respectively. C_{10} means that the average peak AoI should be no greater than the threshold $AoI_{\max}$.

Based on virtual queue [15], the long-term constraints are converted into queue stability constraints. Define the virtual deficit queues of queuing delay corresponding to C_4, C_5, C_6, C_7, C_8, and C_9 as $G_s^l(t)$, $G_s^u(t)$, $G_{Tx}^l(t)$, $G_{Tx}^u(t)$, $G_c^l(t)$, and $G_c^u(t)$. Define the virtual deficit queues of AoI corresponding to C_{10} as $AD(t)$. Virtual deficit queue backlogs are given by

$$G_s^l(t+1) = \Big[G_s^l(t) + \frac{\Theta_s^l(t+1)}{\tilde{K}(t+1)} - \tau_{s,\max}^{l,q}\Big]^+, \tag{30}$$

$$G_s^u(t+1) = \Big[G_s^u(t) + \frac{\Theta_s^u(t+1)}{\tilde{K}(t+1)} - \tau_{s,\max}^{u,q}\Big]^+, \tag{31}$$

$$G_{Tx}^l(t+1) = \Big[G_{Tx}^l(t) + \frac{\Theta_{Tx}^l(t+1)}{\tilde{S}^l(t+1)} - \tau_{Tx,\max}^{l,q}\Big]^+, \tag{32}$$

$$G_{Tx}^u(t+1) = \Big[G_{Tx}^u(t) + \frac{\Theta_{Tx}^u(t+1)}{\tilde{S}^u(t+1)} - \tau_{Tx,\max}^{u,q}\Big]^+, \tag{33}$$

$$G_c^l(t+1) = \Big[G_c^l(t) + \frac{\Theta_c^l(t+1)}{\tilde{C}^l(t+1)} - \tau_{c,\max}^{l,q}\Big]^+, \tag{34}$$

$$G_c^u(t+1) = \Big[G_c^u(t) + \frac{\Theta_c^u(t+1)}{\tilde{C}^u(t+1)} - \tau_{c,\max}^{u,q}\Big]^+, \tag{35}$$

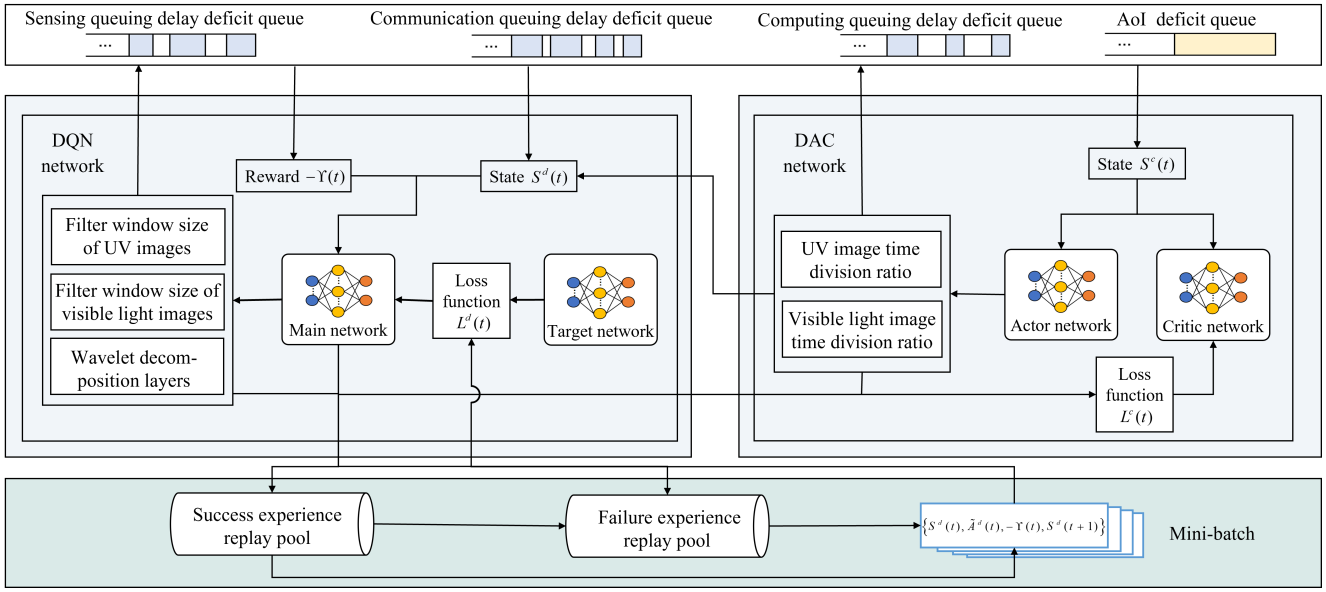

Fig. 5. The framework of multispectral integrated sensing, communication, and computing algorithm based on AoI and false negative aware multi-experience replay cooperative learning.

$$AD(t+1) = \Big[AD(t) + PAoI(t) - AoI_{\max}\Big]^+. \tag{36}$$

Virtual queue backlog characterizes the deviation from the threshold. If virtual queues are mean rate stable, $C_4 \sim C_{10}$ hold automatically [16].

Denoting $\Gamma(t) = \Big[G_s^l(t), G_s^u(t), G_{Tx}^l(t), G_{Tx}^u(t), G_c^l(t), G_c^u(t), AD(t)\Big]$, Lyapunov function is defined as

$$L(\Gamma(t)) = \frac{1}{2}\Big[(G_s^l(t))^2 + (G_s^u(t))^2 + (G_{Tx}^l(t))^2 + (G_{Tx}^u(t))^2 + (G_C^l(t))^2 + (G_C^u(t))^2 + (AD(t))^2\Big]. \tag{37}$$

The one-slot Lyapunov drift is the expected deviation of the Lyapunov function between two adjacent slots, i.e., $\mathbb{E}[L(\Gamma(t+1)) - L(\Gamma(t))|\Gamma(t)]$. Define $\Omega(t) = \alpha_1 PAoI(t) + \alpha_2 FP(t) + \alpha_3 FN(t)$. By minimizing the upper bound of drift, the long-term optimization problem $\mathbf{P1}$ is transformed into a bunch of single-slot sequential optimization problem as

$$\begin{aligned}\mathbf{P2}: \min_{\{w^l(t), w^u(t), \delta^l(t), \delta^u(t), d(t)\}} \quad & \Upsilon(t) = V\Omega(t) \\ & + G_s^l(t)\frac{\Theta_s^l(t+1)}{\tilde{K}(t+1)} + G_s^u(t)\frac{\Theta_s^u(t+1)}{\tilde{K}(t+1)} \\ & + G_{Tx}^l(t)\frac{\Theta_{Tx}^l(t+1)}{\tilde{S}^l(t+1)} + G_{Tx}^u(t)\frac{\Theta_{Tx}^u(t+1)}{\tilde{S}^u(t+1)} \\ & + G_c^l(t)\frac{\Theta_c^l(t+1)}{\tilde{C}^l(t+1)} + G_c^u(t)\frac{\Theta_c^u(t+1)}{\tilde{C}^u(t+1)} \\ & + AD(t)PAoI(t), \\ \text{s.t.} \quad & C_1 \sim C_3, \end{aligned} \tag{38}$$

where V is the weight of $\mathbb{E}\big[\Omega(t)|\Gamma(t)\big]$, which enables adjustable tradeoff between $\Omega(t)$ minimization and queue stability.

IV. Integration Algorithm of Multispectral Sensing, Communication, and Computing Based on AoI and False-Negative Aware Multi-Experience Replay Cooperative Learning

We model the transformed problem as a Markov decision process (MDP). Conventional solutions for MDP problems such as dynamic programming and policy iteration are not applicable due to the following reasons. First, the optimization problem involves both continuous and integer optimization variables, which falls into the category of mixed-integer nonlinear programming and is NP-hard. Second, it is infeasible to derive the state transfer probability of MDP because a priori knowledge of stochastic variables is unknown. Therefore, the model-free DQN is employed as a solution. However, since $\mathbf{P2}$ involves both integer and continuous optimization variables, it cannot be directly solved by conventional DQN. We address this issue by augmenting DQN with a cooperative DAC network, where the continuous output of DAC is incorporated into the state space of DQN to generate integer decision. The dual state space, action space, and reward function of MDP are introduced as follows.

1) Dual State Space: Dual state spaces $\boldsymbol{S}^c(t)$ and $\boldsymbol{S}^d(t)$ are constructed for DAC and DQN, respectively. $\boldsymbol{S}^c(t) = \{G_s^l(t), G_s^u(t), G_{Tx}^l(t), G_{Tx}^u(t), G_c^l(t), G_c^u(t), AD(t), V\}$, which contains virtual deficit queue backlogs of queuing delay and AoI, and the weight of $\mathbb{E}\big[\Omega(t)|\Gamma(t)\big]$. $\boldsymbol{S}^d(t) = \{\boldsymbol{S}^c(t), \tilde{\boldsymbol{A}}^c(t)\}$, where $\tilde{\boldsymbol{A}}^c(t)$ represents the continuous action output of DAC.

2) Action Space: The action space contains continuous space $\boldsymbol{A}^c(t) = \big\{\delta^l(t), \delta^u(t)\big\}$ and integer space $\boldsymbol{A}^d(t) = w^l(t) \otimes w^u(t) \otimes d(t)$, where $\otimes$ is Cartesian product.

3) Reward Function: The reward function is defined as the negative of the optimization objective of $\mathbf{P2}$, i.e., $-\Upsilon(t)$.

The detailed framework of the proposed algorithm is shown in Fig. 5. The edge server constructs a pair of cooperative DAC and DQN to learn the optimal integration strategy of

multispectral sensing, communication, and computing. The DAC consists of an actor network $\boldsymbol{\theta}^{actor}$ and a critic network $\boldsymbol{\theta}^{critic}$, which are utilized to learn the continuous decisions of time division ratios of UV and visible light images. The continuous output of DAC is forwarded as the input of DQN, which combines a main network $\boldsymbol{\theta}^{main}$ and a target network $\boldsymbol{\theta}^{target}$ to learn the integer decisions of filter window size and wavelet decomposition layer.

We further design multi-experience replay pools to improve convergence rate and learning optimality. The multi-experience replay pools consist of a success experience replay pool $\boldsymbol{\mathcal{G}}(t)$ and a failure experience replay pool $\boldsymbol{\mathcal{H}}(t)$. The loss function is calculated to update DQN based on mini-batch extracted from both success and failure pools. The proposed algorithm can achieve fast convergence and reduce probabilistic AoI bound violation and false-negative detection occurrence at initial-learning and post-learning stages respectively by adjusting the cooperative extraction ratio between $\boldsymbol{\mathcal{G}}(t)$ and $\boldsymbol{\mathcal{H}}(t)$.

The proposed algorithm is suitable for practical system with stochastic nature where the global knowledge is unavailable. In addition, the absence of any assumptions about the probability distribution of random variables further enhances its practical value. The implementation procedures are demonstrated in Algorithm 1, which consists of 1) dual action generation; 2) action execution; 3) AoI and false negative-aware multi-experience replay cooperative learning.

1) Dual Action Generation: First, the edge server inputs $\boldsymbol{S}^c(t)$ into $\boldsymbol{\theta}^{actor}$ and draws the continuous actions $\tilde{\boldsymbol{A}}^c(t)$ based on $\boldsymbol{\pi}(\boldsymbol{S}^c(t)|\boldsymbol{\theta}^{actor})$. Then, $\boldsymbol{S}^d(t)$ is generated with $\boldsymbol{S}^c(t)$ and $\tilde{\boldsymbol{A}}^c(t)$. Moreover, the edge server puts $\boldsymbol{S}^d(t)$ into $\boldsymbol{\theta}^{main}$ to draw the integer actions $\tilde{\boldsymbol{A}}^d(t)$ based on $\boldsymbol{Q}(\boldsymbol{S}^d(t), \boldsymbol{A}^d(t), \boldsymbol{\theta}^{main})$ and ε-greedy method.

2) Action Execution: The edge server sends the actions of filter window size and time devision ratios of UV and visible light images to the multispectral camera for image denoising and transmission.

3) AoI and False Negative-Aware Multi-Experience Replay Cooperative Learning: After partial discharge detection, the edge server observes $AoI(t)$, $FP(t)$, $FN(t)$, and updates queue backlogs of $\Theta_s^l(t+1)$, $\Theta_s^u(t+1)$, $\Theta_{Tx}^l(t+1)$, $\Theta_{Tx}^u(t+1)$, $\Theta_c^l(t+1)$, $\Theta_c^u(t+1)$, $G_s^l(t+1)$, $G_s^u(t+1)$, $G_{Tx}^l(t+1)$, $G_{Tx}^u(t+1)$, $G_c^l(t+1)$, $G_c^u(t+1)$, and $AD(t+1)$ as (3), (4), (9), (10), (17), (18), and (30)$\sim$ (36). Then, the edge server calculates reward $-\Upsilon(t)$, transfers to the next state $\boldsymbol{S}^d(t+1)$ and generates a transition $\mathcal{I}(t) = \{\boldsymbol{S}^d(t), \tilde{\boldsymbol{A}}^d(t), -\Upsilon(t), \boldsymbol{S}^d(t+1)\}$.

The proposed algorithm defines success experience and failure experience from the view of AoI bound violation and false negative occurrence, which can both achieve fast convergence from success experience and reduce probabilistic AoI bound violation and false-negative detection occurrence. Define success experience as the transition that peak AoI bound violation and false-negative detection do not occur in the t-th slot, i.e., $PAoI(t) \leq AoI_{\max}$, $FN(t) = 0$. Define failure experience as $PAoI(t) > AoI_{\max}$, or $FN(t) > 0$. Due to the inherent hysteresis of DRL and action coupling over slots, the proposed algorithm constructs failure experience pool $\boldsymbol{\mathcal{H}}(t)$ by taking the past $M_f(t)$ experiences out of $\boldsymbol{\mathcal{G}}(t)$ and putting them into $\boldsymbol{\mathcal{H}}(t)$.

Algorithm 1 Multispectral Integrated Sensing, Communication, and Computing Algorithm based on AoI and False-Negative Aware Multi-experience Replay Cooperative Learning

Input: $\mathcal{T}$, $\boldsymbol{S}^c(1)$, $\boldsymbol{S}^d(1)$.
Output: $\{w^u(t), w^l(t), \delta^u(t), \delta^l(t), d(t)\}$.
For $t = 1, \cdots, T$ **do**
  Dual action drawing:
  Obtain the continuous action $\tilde{\boldsymbol{A}}^c(t)$ of DAC based on $\boldsymbol{\pi}(\boldsymbol{S}^c(t)|\boldsymbol{\theta}^{actor})$ and generate $\boldsymbol{S}^d(t)$.
  Put $\boldsymbol{S}^d(t)$ into $\boldsymbol{\theta}^{main}$ to draw the integer actions $\tilde{\boldsymbol{A}}^d(t)$ based on $\boldsymbol{Q}(\boldsymbol{S}^d(t), \boldsymbol{A}^d(t), \boldsymbol{\theta}^{main})$ and ε-greedy method.
  Action execution:
  Send actions to multispectral camera for image denoising and transmission.
  AoI and false negative-aware multi-experience replay cooperative learning:
  Observe $AoI(t)$, $FP(t)$, $FN(t)$, and updates all queue backlogs.
  Calculate reward $-\Upsilon(t)$, transfer to the next state $\boldsymbol{S}^d(t+1)$ and generate a transition $\mathcal{I}(t) = \{\boldsymbol{S}^d(t), \tilde{\boldsymbol{A}}^d(t), -\Upsilon(t), \boldsymbol{S}^d(t+1)\}$.
  Calculate reward $-\Upsilon(t)$ as (38).
  Update all queue backlogs and transfer to $\boldsymbol{S}^d(t+1)$.
  if $PAoI(t) > AoI_{\max}$, or $FN(t) > 0$
    Construct $\boldsymbol{\mathcal{H}}(t)$ by taking the past $M_f(t)$ experiences out of $\boldsymbol{\mathcal{G}}(t)$ and putting them into $\boldsymbol{\mathcal{H}}(t)$.
  end if
  Calculate the cooperative extraction ratio $\beta(t)$ based on (39) and extract a mini-match $\tilde{\boldsymbol{\mathcal{B}}}(t)$ from $\boldsymbol{\mathcal{G}}(t)$ and $\boldsymbol{\mathcal{H}}(t)$.
  Calculate TD error $\delta(t)$ as (40).
  Calculate loss function $L^d(t)$ and $L^c(t)$ as (41) and (42).
  Update $\boldsymbol{\theta}^{main}$, $\boldsymbol{\theta}^{critic}$, and $\boldsymbol{\theta}^{actor}$.
  Update $\boldsymbol{\theta}^{target} = \boldsymbol{\theta}^{main}$ every T_d slots.
end for

The edge server extracts I_d experiences from both success experience replay pool $\boldsymbol{\mathcal{G}}(t)$ and failure experience replay pool $\boldsymbol{\mathcal{H}}(t)$ to cooperatively construct a mini-batch $\tilde{\boldsymbol{\mathcal{B}}}(t)$. Define the cooperative extraction ratio β, $\beta > 0$, as the ratio of the number of success experiences to that of experiences in $\tilde{\boldsymbol{\mathcal{B}}}(t)$. Define $\beta_{\min}$ and $\beta_{\max}$ as the upper and lower bounds of β. As time slot increasing, $\beta(t)$ keeps decreasing from $\beta_{\max}$ with the step size of η_0 so as to achieve fast convergence speed by exploiting more success experiences at the initial-learning stage, and reduce probabilistic AoI bound violation and false-negative detection occurrence by exploiting more failure experiences at the post-learning stage. When AoI bound violation and false negative occurs, the cooperative extraction ratio β increases with the step size of η_β to improve learning optimality. Therefore, β is given by

$$\beta(t) = \max\Big\{\beta_{\min}, \beta_{\max}(1-\eta_0 t) + \eta_\beta \mathbb{I}\{PAoI(t+1) > AoI_{\max} \text{ or } FN(t) > 0\}\Big\}. \quad (39)$$

$\mathbb{I}\{x\}$ represents the indicator function, where $\mathbb{I}\{x\} = 1$ represents that x is true, and $\mathbb{I}\{x\} = 0$ otherwise.

The temporal-difference (TD) error of DQN are calculated based on both success experiences and failure experiences in $\tilde{\boldsymbol{\mathcal{B}}}(t)$, which is given by

$$\delta(t) = \sum_{\forall(\boldsymbol{S}^d(t),\boldsymbol{A}^d(t))\in\tilde{\boldsymbol{\mathcal{B}}}(t)} [-\Upsilon_b(t) - \boldsymbol{Q}(\boldsymbol{S}^d(t),\boldsymbol{A}^d(t),\boldsymbol{\theta}^{main}) + \gamma_d \max_{\boldsymbol{A}^d(t+1)} \boldsymbol{Q}(\boldsymbol{S}^d(t+1),\boldsymbol{A}^d(t+1),\boldsymbol{\theta}^{target})], \quad (40)$$

where $\gamma_d \in (0,1]$ is the DQN discount factor.

The loss function utilized to measure the learning performance of DQN is calculated as

$$L^d(t) = (\delta(t))^2. \quad (41)$$

Since the continuous output of DAC is part of the state space for DQN, the Q value output by DQN, which quantifies state-action value, is utilized to measure the learning performance of DAC. Specifically, given the same action, a larger Q value indicates that the state is more superior for reducing AoI and avoiding false-negative detection. Therefore, the loss function of DAC is defined as the average Q value of DQN with $\tilde{\boldsymbol{A}}^c(t)$ as part of the state, which is given by

$$L^c(t) = -\frac{1}{|\boldsymbol{A}^d(t)|} \sum_{\tilde{\boldsymbol{A}}^d(t)\in\boldsymbol{A}^d(t)} Q(\boldsymbol{S}^d(t),\tilde{\boldsymbol{A}}^d(t),\boldsymbol{\theta}^{main} \mid \tilde{\boldsymbol{A}}^c(t)), \quad (42)$$

where $|\boldsymbol{A}^d(t)|$ represents the size of $\boldsymbol{A}^d(t)$.

Finally, edge server updates the main network θ^{main}, actor network $\boldsymbol{\theta}^{actor}$ and critic network $\boldsymbol{\theta}^{critic}$ with gradient descent algorithm. The target network $\boldsymbol{\theta}^{target}$ is updated every $T_d > 1$ slots as $\boldsymbol{\theta}^{target} = \boldsymbol{\theta}^{main}$.

TABLE II
SIMULATION PARAMETERS

Parameter	Value	Parameter	Value
$W_{\min}, W_{\max}$	$3, 9$	$d_{\min}, d_{\max}$	$3, 6$
$A_c^l(t,k), A_c^u(t,k)$	0.1, 0.2 Mbits	$K(t)$	15
$f_s^u(t), f_s^l(t)$	1.2 GHz	τ, T_d	1 s, 20
$R(t)$	7 Mbits/s	$AoI_{\max}$	0.2 s
$\alpha_1, \alpha_2, \alpha_3$	$10, 1, 10$	$\beta_{\min}, \beta_{\max}$	0.1, 0.2
η_0, η_β	0.02, 0.05	γ_d	0.99

V. SIMULATION RESULTS

In simulation, 800 frames of UV and visible light images captured in practical high-voltage substations are utilized to construct the sample base and validate the effectiveness of the proposed algorithm. The detailed simulation parameters are summarized in Table II [17], [18]. The proposed algorithm can be extended to new data sets by dynamically adjusting the optimization policy based on performance feedbacks. Moreover, success and failure experiences of new data sets can be extracted and combined to enhance learning capability, increasing convergence rate, and reducing probabilistic AoI bound violation and false-negative detection occurrence. The simulation environment is constructed by MATLAB and run over ThinkStation P520 with Intel Core i7-6900K CPU and 48 GB random access memory.

TABLE III
ANALYSIS OF EXPERIMENTAL RESULTS

		$PAoI(t)$ (ms)	$FP(t)$	$FN(t)$
Experiment I	Proposed	194.0	1.85	0
	DDPG	217.0	5.53	3.87
	EE	190.8	16.47	4.98
	AG	186.7	15.10	6.12
Experiment II	Proposed	183.7	0.80	0
	DDPG	222.9	2.47	0
	EE	155.2	16.55	5.16
	AG	148.0	14.93	6.07
Experiment III	Proposed	194.7	1.87	0
	DDPG	236.5	1.42	0
	EE	161.7	16.59	5.11
	AG	161.4	14.97	6.18

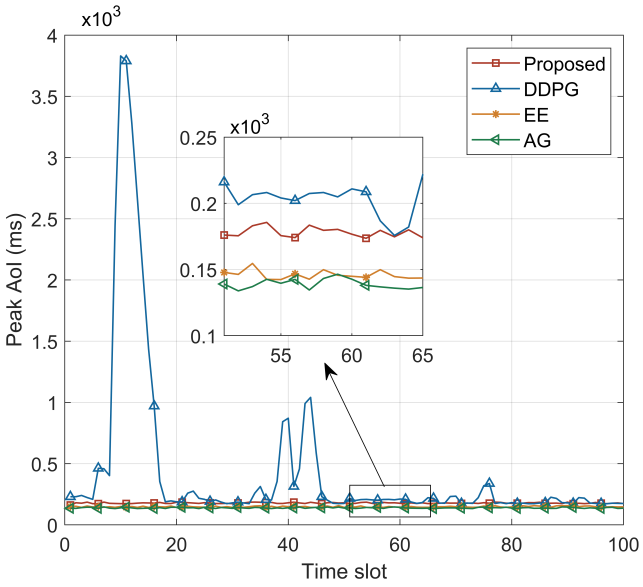

Fig. 6. Peak AoI versus time slots.

Three state-of-art algorithms are employed for comparison. The first one is the deep deterministic policy gradient algorithm (DDPG) [19]. The optimization objective and variables of DDPG are the same as the proposed algorithm. The second one is the expert experience algorithm (EE) [17], where filtering window size and wavelet decomposition level are determined as $\omega^u(t) = \omega^l(t) = 3$ and $d(t) = 4$ based on expert experience. The third one is the age-greedy algorithm (AG) [20]. Filtering window size and wavelet decomposition level of AG are set as the minimum values to aggressively minimize AoI. Both EE and AG aim to minimize the peak AoI by optimizing time division ratio.

A total of three experiments are carried out. In each slot, $K(t)$ frames of images are randomly extracted from the sample base as the inputs of $\Theta_s^l(t)$ and $\Theta_s^u(t)$. Table III presents the performances of three experiments. Compared

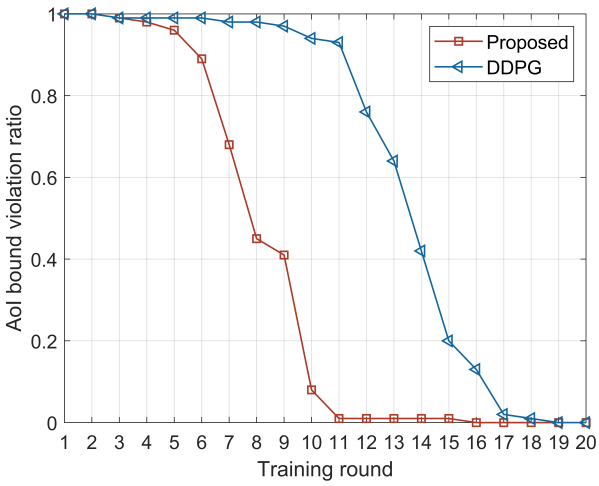

Fig. 7. AoI bound violation ratio versus training round.

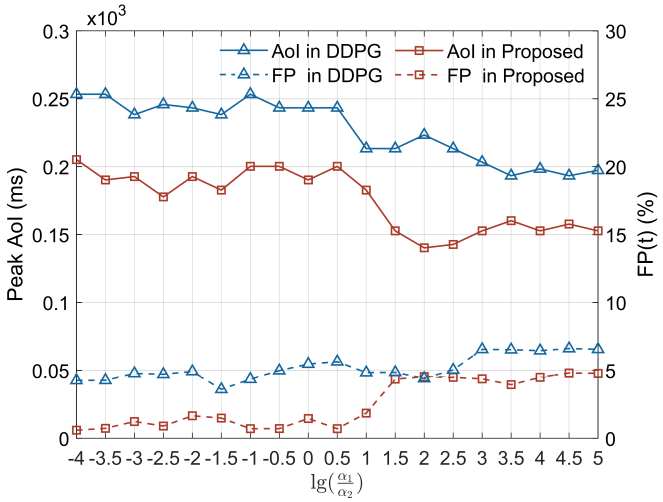

Fig. 8. Impact of $\frac{\alpha_1}{\alpha_2}$ on the peak AoI and false-positive detection ratio.

with EE, numerical results of three experiments show that the proposed algorithm reduces false-positive detection ratio by 90.89% at the cost of 11.30% peak AoI increment on average. Additionally, the false-negative detection ratio of the proposed algorithm remains as 0 throughout three experiments, which verifies its guarantee capability of detection accuracy.

1) Comparison of Convergence: Fig. 6 presents the peak AoI based on experiment III. Fig. 7 shows the AoI bound violation ratio versus training round. Each round consists of 100 slots. Peak AoI of the proposed algorithm converges to 178.3 ms and the average peak AoI is reduced by 59.62% compared with DDPG. Besides, the AoI bound violation ratio of the proposed algorithm is reduced to 1% after 11 training rounds and reduced to 0 after 16 training rounds. The required training rounds of the proposed algorithm are 38.89% and 15.79% lower than those of DDPG. The superior performances stem from the adjustable cooperative extraction ratio $\beta(t)$. Specifically, based on (39), the proposed algorithm reduces $\beta(t)$ from $\beta_{\max}$ to $\beta_{\min}$ with the step size of η_0, which enables it to adopt a larger extraction ratio of success experience for improving convergence speed at the initial-learning stage, and adopt a larger extraction ratio of failure experience at the post-learning stage to reduce probabilistic AoI bound violation and false-negative detection occurrence from failure experience. Moreover, when AoI bound violation occurs, $\beta(t)$ is increased with the step size of η_β to improve learning optimality by extracting more success experience.

2) Comparison of Detection Timeliness and Accuracy: The impacts of different $\frac{\alpha_1}{\alpha_2}$ and $\frac{\alpha_1}{\alpha_3}$ on the peak AoI, false-positive detection ratio, and false-negative detection ratio are respectively shown in Fig. 8 and Fig. 9. A larger $\frac{\alpha_1}{\alpha_2}$ and $\frac{\alpha_1}{\alpha_3}$ indicate that the proposed algorithm pays more attention to improving detection timeliness. As $\frac{\alpha_1}{\alpha_2}$ increasing from 10^{-4} to 10^5, the proposed algorithm increases the false-positive detection ratio from 0.64% to 4.78% while decreasing peak AoI from 205.2 ms to 152.7 ms. Therefore, $\frac{\alpha_1}{\alpha_2}$ should be carefully selected to avoid prohibitive false-positive detection ratio and achieve great AoI performance simultaneously. Al-

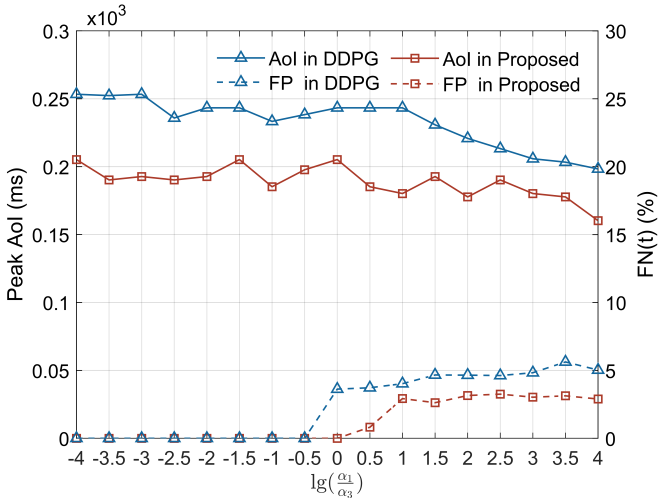

Fig. 9. Impact of $\frac{\alpha_1}{\alpha_3}$ on the peak AoI and false-negative detection ratio.

though the false-negative detection ratio increases with $\frac{\alpha_1}{\alpha_3}$, the proposed algorithm has the best trade-off between false-negative detection ratio and peak AoI. The reason can be elaborated based on *Remark 2*, i.e., more emphasis are put on reducing AoI by utilizing smaller filtering window size and decomposition level, which deteriorates the qualities of image denosing and image fusion, and results in higher false-negative detection ratio. However, the proposed algorithm benefits from the AoI and false-negative awareness, which helps to trade off the detection timeliness and accuracy better. The proposed algorithm sheds insight on how to select $\frac{\alpha_1}{\alpha_3}$ and $\frac{\alpha_1}{\alpha_2}$ for practical application, e.g., $\frac{\alpha_1}{\alpha_2} = 10$ and $\frac{\alpha_1}{\alpha_3} = 1$ achieve superior performances in both peak AoI and detection accuracy. Based on above analysis, α_1, α_2, and α_3 are effectively selected as 10, 1, 10 in the following simulations.

3) Impact of Sensing-Layer Frame Rate: Fig. 10 shows the impact of frame rate, i.e., $\frac{K(t)}{\tau}$, on the peak AoI and end-to-end delay. An important finding is that AoI is not always consistent with end-to-end delay, which is mentioned

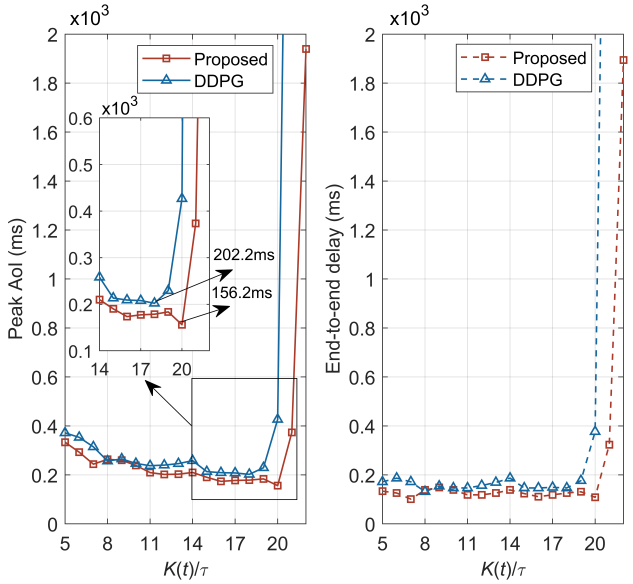

Fig. 10. Impact of frame rate $\frac{K(t)}{\tau}$ ($V = 7, \alpha_1 = 10, \alpha_2 = 1, \alpha_3 = 10$, $f_s^l(t) = f_s^u(t) = 1.2$ GHz).

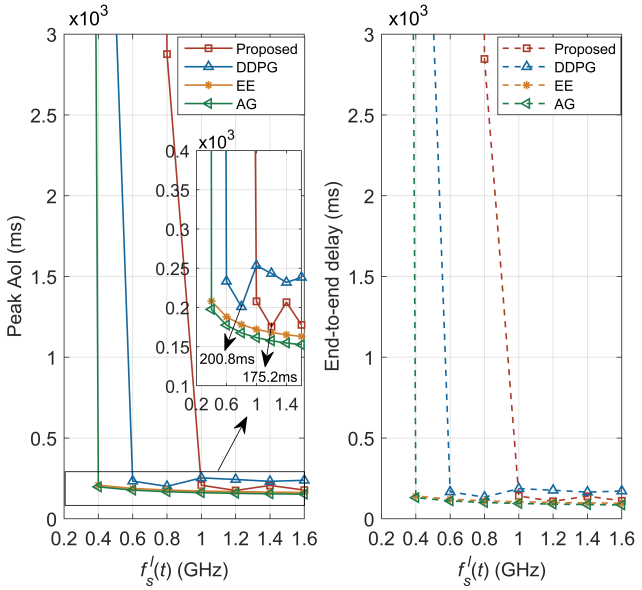

Fig. 11. Peak AoI and end-to-end delay versus sensing-layer computing resource $f_s^l(t)$ ($V = 7, \alpha_1 = 10, \alpha_2 = 1, \alpha_3 = 10$, $\frac{K(t)}{\tau} = 15$ FPS).

in Remark 1. As frame rate increasing from 5 to 20 FPS, the end-to-end delay increases continuously while the peak AoI firstly falls down and then rises. Such results agree with the mathematical analysis in (26) and (27). In the low frame-rate case, e.g., $\frac{K(t)}{\tau} \in [5, 20]$ FPS, increasing $K(t)$ can reduce peak AoI by reducing $\frac{\tau}{K(t-1)}$. In the high frame-rate case, e.g., $\frac{K(t)}{\tau} > 20$ FPS, peak AoI is determined by end-to-end delay of two consecutive frames based on (26) and (27). As $\frac{K(t)}{\tau}$ increasing, more frames of images are backlogged in the queue, which results in end-to-end delay increasing. Therefore, increasing $K(t)$ results in substantial increment of peak AoI in the high frame-rate case.

4) Impact of Sensing-Layer Computing Resource: Fig. 11 shows the impact of sensing-layer computing resource, i.e., $f_s^l(t)$, on the peak AoI and end-to-end delay. As $f_s^l(t)$ increasing from 0.2 to 1.6 GHz (FPS= 15), the end-to-end delay and the peak AoI gradually decrease. When the sensing-layer computing resource is large enough, the peak AoI does not continue to decrease due to the limitation of sensing-layer queue of storage images, and similarly the AoI converges to a stable value since frame dropping events do not occur.

5) Impact of Computing-Layer Computing Resource: Fig. 12 shows the impact of computing-layer computing resource, i.e., $f_c(t)$, on the peak AoI and false-positive detection ratio. As $f_c(t)$ increasing from 1.6 to 4 GHz, the peak AoI firstly firstly drops quickly and then slows down, and the proposed algorithm performs best in the false-positive detection ratio. When the computing-layer computing resource is large enough, the peak AoI does not continue to decrease because timely processing of fused images is required. When $f_c(t) = 3.7$ GHz, compared with DDPG, the proposed algorithm reduces the peak AoI and false-positive detection ratio by 8.69% and 68.20%, respectively.

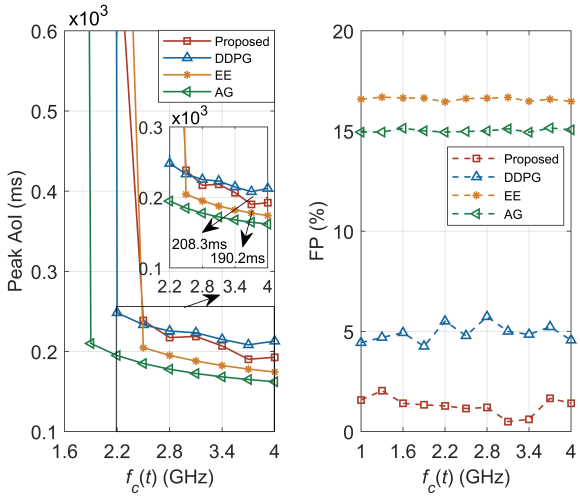

Fig. 12. Peak AoI and false-positive detection ratio versus computing-layer computing resource $f_c(t)$ ($V = 7, \alpha_1 = 10, \alpha_2 = 1, \alpha_3 = 10$, $f_s^l(t) = f_s^u(t) = 1.2$ GHz, $\frac{K(t)}{\tau} = 15$ FPS).

VI. Conclusion

In this paper, we constructed a framework of integrated sensing, communication, and computing for partial discharge detection based on multispectral images. We developed peak AoI to characterize timeliness, and employed false-positive and false-negative detection ratios to characterize accuracy. Then, timeliness and accuracy were jointly guaranteed by the design of optimization problem and proposed algorithm. In addition, the proposed algorithm based on DAC-DQN cooperation leveraged multi-experience replay pools and adaptive mini-batch extraction to facilitate cooperative learning. Compared with DDPG, the proposed algorithm reduces the peak AoI by 59.62%. Compared with EE and AG, the proposed algorithm achieves the minimum false-positive detection ratio

and false-negative detection ratio. An important finding is that average peak AoI and end-to-end delay increased inconsistently with frame rate, which sheds insight on trade-off design between timeliness and low latency. Future work will consider multimodal semantic communication to further reduce peak AoI for partial discharge detection based on multispectral images.

ACKNOWLEDGEMENTS

This paper was funded by the Science and Technology Project of State Grid Corporation of China under Grant Number 5700-202358611A-3-2-ZN.

REFERENCES

[1] Z. Guo, Q. Ye, Y. Wang *et al.*, "Study of the development of negative DC corona discharges on the basis of visible digital images," *IEEE Trans. Plasma Sci.*, vol. 48, no. 7, pp. 2509–2514, July 2020.

[2] M. M. de Lucena and A. Augusto Fröhlich, "Modeling misbehavior detection timeliness in vanets," in *2022 IEEE 27th International Conference on Emerging Technologies and Factory Automation (ETFA)*, 2022, pp. 1–8.

[3] Z. Zhou, Z. Jia, H. Liao *et al.*, "Secure and latency-aware digital twin assisted resource scheduling for 5G edge computing-empowered distribution grids," *IEEE Trans. Ind. Inf.*, vol. 18, no. 7, pp. 4933–4943, July 2022.

[4] Z. Wang, X. Mu, Y. Liu *et al.*, "Noma-aided joint communication, sensing, and multi-tier computing systems," *IEEE J. Sel. Areas Commun.*, vol. 41, no. 3, pp. 574–588, Mar. 2023.

[5] Q. Qi, X. Chen, A. Khalili *et al.*, "Integrating sensing, computing, and communication in 6G wireless networks: Design and optimization," *IEEE Trans. Commun.*, vol. 70, no. 9, pp. 6212–6227, Sept. 2022.

[6] T. Rajat, K. Sertac, and M. Eytan, "Improving age of information in wireless networks with perfect channel state information," *IEEE/ACM Trans. on Networking*, vol. 28, no. 4, pp. 1765–1778, Aug. 2020.

[7] H. Hu, K. Xiong, G. Qu *et al.*, "AoI-minimal trajectory planning and data collection in UAV-assisted wireless powered IoT networks," *IEEE Internet Things J.*, vol. 8, no. 2, pp. 1211–1223, Jan. 2021.

[8] D. Sinha and R. Roy, "Scheduling status update for optimizing age of information in the context of industrial cyber-physical system," *IEEE Access*, vol. 7, pp. 95 677–95 695, 2019.

[9] Z. Zhou, X. Chen, H. Liao *et al.*, "Collaborative learning-based network resource scheduling and route management for multi-mode green IoT," *IEEE Trans. Green Commun. Networking*, vol. 7, no. 2, pp. 928–939, June 2023.

[10] L. Liu, K. Xiong, J. Cao *et al.*, "Average AoI minimization in UAV-assisted data collection with RF wireless power transfer: A deep reinforcement learning scheme," *IEEE Internet Things J.*, vol. 9, no. 7, pp. 5216–5228, Apr. 2022.

[11] M. Li, C. Chen, H. Wu, X. Guan, and X. Shen, "Age-of-information aware scheduling for edge-assisted industrial wireless networks," *IEEE Trans. Ind. Inf.*, vol. 17, no. 8, pp. 5562–5571, Nov. 2021.

[12] S. Lee and D.-H. Choi, "Federated reinforcement learning for energy management of multiple smart homes with distributed energy resources," *IEEE Trans. Ind. Inf.*, vol. 18, no. 1, pp. 488–497, Jan. 2022.

[13] M. Kamruzzaman, J. Duan, D. Shi, and M. Benidris, "A deep reinforcement learning-based multi-agent framework to enhance power system resilience using shunt resources," *IEEE Trans. Power Syst.*, vol. 36, no. 6, pp. 5525–5536, May 2021.

[14] C.-F. Liu, M. Bennis, M. Debbah *et al.*, "Dynamic task offloading and resource allocation for ultra-reliable low-latency edge computing," *IEEE Trans. Commun.*, vol. 67, no. 6, pp. 4132–4150, June 2019.

[15] H. Liao, Z. Zhou, X. Zhao *et al.*, "Learning-based queue-aware task offloading and resource allocation for space-air-ground-integrated power IoT," *IEEE Internet Things J.*, vol. 8, no. 7, pp. 5250–5263, Apr. 2021.

[16] M. J. Neely, *Stochastic Network Optimization With Application to Communication and Queueing Systems*. San Rafael, CA, USA: Morgan and Claypool, 2010.

[17] L. Jin, J. Chen, W. Zhang, and S. Yan, "Partial discharge ultraviolet imaging detection of power equipment based on image processing technology," *Power System Protection and Control*, vol. 41, no. 8, pp. 43–48, Apr. 2013.

[18] H. Liao, Z. Zhou, X. Zhao, L. Zhang, S. Mumtaz, A. Jolfaei, S. H. Ahmed, and A. K. Bashir, "Learning-based context-aware resource allocation for edge-computing-empowered industrial iot," *IEEE Internet Things J.*, vol. 7, no. 5, pp. 4260–4277, May 2020.

[19] M. Samir, C. Assi, S. Sharafeddine *et al.*, "Age of information aware trajectory planning of UAVs in intelligent transportation systems: A deep learning approach," *IEEE Trans. Veh. Technol.*, vol. 69, no. 11, pp. 12 382–12 395, Nov. 2020.

[20] Y. Shao, Q. Cao, S. C. Liew *et al.*, "Partially observable minimum-age scheduling: The greedy policy," *IEEE Trans. Commun.*, vol. 70, no. 1, pp. 404–418, Jan. 2022.

Haijun Liao (Student Member, IEEE) received the B. Eng. degree in smart grid information engineering in 2019 from North China Electric Power University, Beijing, China, where she is currently working toward the Ph.D. degree in electrical engineering with the School of Electrical and Electronic Engineering, North China Electric Power University. Her research interests include cloud-edge-end collaborative computing offloading in power Internet of Things. She was the recipient of the IEEE IWCMC 2019 Best Paper Award, IEEE VTC-2020 Spring Best Student Paper Award, and IEEE CAMAD 2021 Best Paper Award.

Zijia Yao received the B. Eng. degree in electrical engineering in 2023 from North China Electric Power University, Beijing, China, where she is currently working toward the Ph.D. degree in electrical engineering with the School of Electrical and Electronic Engineering, North China Electric Power University. Her interests include smart grid energy management and power internet of things.

Jiaxuan Lu majored in communication engineering with the School of Electrical and Electronic Engineering, North China Electric Power University, Beijing, China. His research focuses on power Internet of Things.

Yiling Shu received the B.Eng. degree in communication engineering in 2022 from North China Electric Power University, Beijing, China, where he is currently working toward the M.E. degree in information and communication engineering with the School of Electrical and Electronic Engineering, North China Electric Power University. His research interest is power wireless communication networks and power internet of things.

Zhenyu Zhou (Senior Member, IEEE) received the M.E. and Ph.D. degrees in international information and communication studies from Waseda University, Tokyo, Japan, in 2008 and 2011, respectively. From 2012 to 2019, he was an Associate Professor with the School of Electrical and Electronic Engineering, North China Electric Power University, Beijing, China, where he has been a Full Professor since 2019. His research interests include power Internet of Things, smart grid information and communication, communication-sensing-computing integration, and smart grid energy management. He was the recipient of the IET Premium Award in 2017, IEEE Globecom 2018 Best Paper Award, IEEE International Wireless Communications and Mobile Computing Conference 2019 Best Paper Award, and IEEE Communications Society Asia-Pacific Board Outstanding Young Researcher. He was an Associate Editor for IEEE Internet of Things Journal, IET Quantum Communication, IEEE Access, and EURASIP Journal on Wireless Communications and Networking, and the Guest Editor of IEEE Communications Magazine, IEEE Transactions on Industrial Informatics, and Transactions on Emerging Telecommunications Technologies. He is an IET Fellow and a Senior Member of the Chinese Institute of Electronics and the China Institute of Communications.

Shahid Mumtaz (Senior Member, IEEE) received the master's and Ph.D. degrees in electrical and electronic engineering from the Blekinge Institute of Technology, Karlskrona, Sweden, and University of Aveiro, Aveiro, Portugal, in 2006 and 2011, respectively. He has more than 12 years of wireless industry/academic experience. Since 2011, he has been with the Instituto de Telecomunicac¸ ˜oes, Aveiro, Portugal, where he currently holds the position of Auxiliary Researcher and adjunct positions with several universities across the Europe-Asian Region. He is currently also a Visiting Researcher with Nokia Bell Labs, Murray Hill, NJ, USA. He is the author of 4 technical books, 12 book chapters, and more than 150 technical papers in the area of mobile communications. Dr. Mumtaz is an ACM Distinguished Speaker, Editor-in-Chief for IET Journal of Quantum Communication, Vice Chair of Europe/Africa Region IEEE ComSoc: Green Communications and Computing society, and Vice Chair for IEEE standard on P1932.1, Standard for Licensed/Unlicensed Spectrum Interoperability in Wireless Mobile Networks.